Effect of trivalent rare earth doping in cadmium silicates hosts: A theoretical study

Eduily Benvindo Vaz Freire[1,*], Anderson Lira de Sales Santos[1], Giordano Frederico da Cunha Bispo[2], Zélia Soares Macedo[1,2], Robert A Jackson[3], and Mário Ernesto Giroldo Valerio[1]

[1] Physics Department, Federal University of Sergipe, 49100-000, São Cristovão, SE, Brazil.

[2] Materials Science and Engineering Department, Federal University of Sergipe, 49100-000, São Cristovão-SE, Brazil.

[3] School of Chemical and Physical Science, Keele University, Keele, Staffordshire ST5 5BG, UK.

[*]E-mail: eduily.vaz@gmail.com

Abstract

The objective of the present work is to study most of the possibilities for extrinsic defects in the three cadmium silicate matrices, $CdSiO_3$, Cd_2SiO_4 and Cd_3SiO_5 and understand the final geometry of the most energetically favourable defects, which are generators of the luminescence centres in the material. This analysis will be performed out through classical and static computer modelling, using the code GULP. We examined a large number of reactions that can occur when we incorporate trivalent rare earth ions (R^{3+}) in these structures, and analysed the insertion of dopants in all symmetrically non-equivalent sites for three structures. Results demonstrated that R ions have a preference by Cd sites and cadmium vacancy are created in order to compensate charge unbalance. We carefully investigated different distances

and angles between the ions involved in the defects formation for $CdSiO_3$ and found that all investigated R3+ ions have the same lower energetic defect configuration. We found a configuration preference for rare earth ions in an array with a distance of around 7 Å and an angle closer to 180º. These results predict a possible set of two dipoles caused by position of cadmium vacancy in defect.

Keyword: Cadmium silicate, $CdSiO_3$, Extrinsic defects, Mott–Littleton method, Trivalent dopants.

Introduction

Materials that have persistent luminescence characteristic have been widely studied since the beginning of the 20th century [1], mainly due to the wide possibilities of their applications. A long emission lifetime added to high brilliance allows several opportunities as emergency signs, luminous ceramics, energy conserving devices, scintillators, bioimaging, photocatalytic among others [2–6]. Sulphites were the first persistent emission materials studied, but problems such as chemical instability and short lifetime limited the applications [7]. By the 1990s, $SrAl_2O_4$:Eu,Dy was successfully developed giving properties like extreme brightness, long duration of emission and chemical stability. Since then, many aluminates and silicates doped with rare earth ions (R) have been reported as potential persistent materials for several applications [8–11]. Among these, cadmium silicates have been reported as a potential material yielding moderate and strong emissions [12].

Cadmium silicates were found in three known crystalline phases, $CdSiO_3$ [13], Cd_2SiO_4 and Cd_3SiO_5 [14], the first host is the most extensively studied due to interesting optical properties already reported in literature. Undoped $CdSiO_3$ has shown to present persistent luminescence even without doping [4,15] with emissions in three visible regions of the spectrum: 590 nm, 490 nm and 406 nm [15]. Such emissions change according to pH used in production allowing a tailored luminescent colour [15]. Previous modelling paper identified the pseudo CdO Schottky defects as the most favourable in this matrix yielding a silicon defect in the lattice [16]. Both can be responsible for these different emissions.

An important aspect to be highlighted is the fact that doping with R^{3+} in the $CdSiO_3$ host covers most of the visible light spectrum, starting from indigo blue to red, just by

changing the R doping ion [10,12,17]. This fact is of great interest because it is possible to choose the doping ion according to the desired luminescence colour and purpose. Persistent emission presented by a doped host spans from few minutes up to hours after the source is removed depending on the R^{3+} dopant [17]. For example, $CdSiO_3$:Sm^{3+} has a pink light emission that can last up to 5 hours and can be see with the naked eye [18] while $CdSiO_3$:Tb^{3+} has a typical green persistent colour [12].

Cd_2SiO_4 stoichiometry also present persistent luminescence when doped with Pr^{3+} ions yielding an almost pure red emission. This is in contrast to Cd_2SiO_4:Tb^{3+} that presents typical green emission from Tb^{3+} without delay in emission [19]. The authors affirm that the lower band gap energy regarding $CdSiO_3$ puts Tb excited levels within the conduction band making Tb persistent emission absent, also affirm that Tb^{3+} substitutes Cd^{2+} ions in the matrix without major distortion of the lattice, despite needing mechanisms for charge compensation [19].

Although the persistent emission is well-known in literature, the mechanisms behind this emission is not clear yet. The presence of R^{3+} in the Cd^{2+} sites is confirmed by EXAFS measurements [19], but the exact nature of the defect responsible for charge compensation still not clear. Therefore, studies with theoretical calculations are needed mainly taking account of all defects related. In this work, we will use classical atomistic computer modelling to conduct a theoretical study of the cadmium silicate family doped with trivalent R ions. This doping study is based on previous works on other materials which provided an understanding about defects from the point of view of formation, structure distortions and energetic aspects [20–25].

Methodology

The methodology used in this work is the classical atomistic modelling, which is based on interatomic potentials to describe the interactions between ions, aiming at minimising energy through the reduction of interatomic forces. For this purpose, we use the well-known GULP program (General Utility Lattice Program) [26]. The set of potential parameters used is based on two interatomic potentials (Buckingham and three body) plus shell model for oxygen ion polarisation. Such potential parameters were previously published in the references [16,20,25]. These sets of interatomic potentials were obtained by fitting the potential parameters to the $CdSiO_3$, Cd_2SiO_4 and Cd_3SiO_5 structures as well as their CdO and SiO_2 precursor oxides[16]. The set of potential parameters for all rare earth oxides (R_2O_3) was obtained from refs [20,25] to describe the doping ions.

Defect formation energies in the compounds were calculated using the Mott-Littleton method [27]. This method divides the crystal into two regions, where in the first region all relaxations of the ions are treated explicitly. The second region is subdivided into region II A, where the ions undergo small displacements based on the relaxations that occurred in the explicit region I, and region II B which is treated as a continuous dielectric. Consistent region sizes of 16 and 22 Å for regions I and IIA were found in the calculations after tests to ensure that convergence had been reached.

For calculations, it was firstly assumed that each defect is isolated in an infinite matrix that yields a good approximation for diluted systems, where the interactions among dopants can be neglected. In these cases, the dopant concentrations are low enough to consider each defect homogeneously distributed in the host lattice [28]. Formation

energies are calculated for all dopants and point defect related to the charge compensation mechanisms.

The simple comparison of the energetic costs using only the formation energies is not strictly correct because this does not take into account the overall mechanisms of the substitution process. One way and by far the most common way is using solid state reactions where all energy terms involved were built up, and these are the so-called solution energies [20]. A great advantage of this methodology is that it can analyse a wide range of combinations of all possible defects without any 'a priori' assumption.

The defects studied here will be defects induced by the presence of ions that did not originally exist in the lattice, the so-called extrinsic defects. These defects are formed by combinations of vacancies, interstitial ions and doping ions that interact via solid state reactions.

The structures were modelled at two different temperatures: i-) 0 K, meaning that the internal energies are the calculated ones without considering the lattice vibrations, and ii-) 300 K, which is normally closer to the experimental conditions, where lattice vibrations were included in the Helmholtz free energies via the harmonic approximation. The theory for including the temperature implemented in the GULP program is described in detail in ref [29].

Considering the doping processes, there are basically two options for the inclusion of doping ion in a solid: i-) the substitutional mechanism, where the dopant can assume the position of a regular ion in the host, replacing the original ion, in a, and, ii-) the interstitial doping, where the dopant ion occupies positions that are not normally occupied by the constituent ions of the matrix, i.e., at interstitial sites. The interstitial doping mechanism is normally found for light ions and neutral elements, like Li+ ions in solid-

state battery materials or atomic H in metals. For heavier elements, interstitial doping is less probable due to the large lattice distortion that would be needed and substitutional doping is more likely to occur.

In the present work, the inclusion of the dopant ions was considered via substitutional doping. There are two possibilities for cationic substitution, in the Si and Cd sites and since the R ions are considered to be in their trivalent states, the substitutions at both cationic sites are aliovalent substitution requiring charge compensation to keep the neutrality of the crystal lattice.

Considering all these aspects, the next step is to devise the possible mechanisms for incorporating the dopants and the corresponding solid-state reaction. The criterion used here in choosing these mechanisms and the reactions was to considered the simplest possible scheme for a particular mechanism that would involve the least number of basic defects in the composition, as a form of charge compensation. The charge compensation defects considered were vacancies, interstitial sites of one of the three ions composing the lattice, Cd, Si or O, and Cd – Si anti-sites. The mechanism and reactions considered in this work are shown in Table 1, where Kröger-Vink notation was employed [30]. From these reactions, it is possible to devise the corresponding energetic balance that gave rise to the solution energies. As an example, the first mechanism in Table 1 is related to the incorporation of the trivalent dopant substitutional at the Cd site being compensated by Cd vacancy. Since a trivalent dopant sitting at a site that would be expected to have a divalent dopant will produce a +1 effective charge, a Cd vacancy will give a -2 effective charge. So, to balance out, the reaction will need two trivalent dopants for each Cd vacancy. The solution energy will thus require twice the energy of a substitutional defect added to the formation energy of a Cd vacancy. However, the dopant has to enter into the system in some form and it is considered that the oxide form is the adequate from the

synthesis point of view. As a result, 3 CdO molecules will be added to the system and within the Mott-Littleton modelling these are considered to contribute to form extra layers of the matrix far from the defect (formally, the CdO ions are moved to infinity). Combining all these energetic terms will give the solution energy of this particular defect.

Some issues have to be considered in constructing the possible defects involved in the doping processes. The first one is the location of the interstitial positions in the silicate matrixes and that was done previously and is described in detail in reference [16]. The same interstitial positions were used here. The second issue is that in the three cadmium silicate structures there are different numbers of Cd, Si and O non-equivalent sites and when vacancies are involved all possible sites should be considered. This will be discussed in the next section.

Table 1: Defect schemes with the corresponding solid-state reactions and the solution energy equations for the calculated extrinsic defects, both for the unbound and bound defects. R indicates the trivalent doping ion.

	$2R_{Cd}^{\bullet} + V''_{Cd}$
Reaction I	$R_2O_3 + 3Cd_{Cd} \rightarrow (2R_{Cd}^{\bullet} + V''_{Cd}) + 3CdO$
Solution energy I	
Unbound defect:	$E_{sol} = 2E_{form}(R_{Cd}^{\bullet}) + E_{form}(V''_{Cd}) + 3E_{Lattice}(CdO) - E_{Lat}$
Bound defect:	$E_{sol} = E_{form}(2R_{Cd}^{\bullet} - V''_{Cd}) + 3E_{Lattice}(CdO) - E_{Lattice}(R_2O_3$
	$4R_{Cd}^{\bullet} + V''''_{Si}$
Reaction II	$2R_2O_3 + 4Cd_{Cd} + Si_{Si} \rightarrow (4R_{Cd}^{\bullet} + V''''_{Si}) + SiO_2 + 4CdO$
Solution energy II	
Unbound defect:	$E_{sol} = 4E_{form}(R_{Cd}^{\bullet}) + E_{form}(V''''_{Si}) + E_{lattice}(SiO_2) + 4E_{lat}$

Bound defect:	$E_{sol} = E_{form}(4R^{\bullet}_{Cd} + V^{''''}{}_{Si}) + E_{lattice}(SiO_2) + 4E_{lattice}(CdC$
	$2R^{\bullet}_{Cd} + O''_{I}$
Reaction III	$R_2O_3 + 2Cd_{Cd} \rightarrow (2R^{\bullet}_{Cd} + O''_{I}) + 2CdO$
Solution energy III	
Unbound defect:	$E_{sol} = 2E_{farm}(R^{\bullet}_{Cd}) + E_{form}(O^{''}{}_{I}) + 2E_{lattice}(CdO) - E_{lattic}$
Bound defect:	$E_{sol} = E_{form}(2R^{\bullet}_{Cd} + O^{''}{}_{I}) + 2E_{lattice}(CdO) - E_{lattice}(R_2O_3)$
	$2R'_{Si} + Cd^{\bullet\bullet}{}_{I}$
Reaction IV	$R_2O_3 + 2Si_{Si} + CdO \rightarrow (2R'_{Si} + Cd^{\bullet\bullet}_{I}) + 2SiO_2$
Solution energy IV	
Unbound defect:	$E_{sol} = 2E_{form}(R^{'}{}_{Si}) + E_{form}(Cd^{\bullet\bullet}_{I}) - E_{lattice}(CdO) + 2E_{latti}$
Bound defect:	$E_{sol} = E_{form}(2R^{'}{}_{Si} + Cd^{\bullet\bullet}_{I}) - E_{lattice}(CdO) + 2E_{lattice}(SiO_2)$
	$4R'_{Si} + Si^{\bullet\bullet\bullet\bullet}{}_{I}$
Reaction V	$2R_2O_3 + 4Si_{Si} \rightarrow (4R'_{Si} + Si^{\bullet\bullet\bullet\bullet}_{I}) + 3SiO_2$
Solution energy V	
Unbound defect:	$E_{sol} = 4E_{form}(R^{'}{}_{Si}) + E_{form}(Si^{\bullet\bullet\bullet\bullet}_{I}) + 3E_{lattice}(SiO_2) - 2E_{la}$
Bound defect:	$E_{sol} = E_{form}(4R^{'}{}_{Si} + Si^{\bullet\bullet\bullet\bullet}_{I}) + 3E_{lattice}(SiO_2) - 2E_{lattice}(R_2$
	$2R'_{Si} + V^{\bullet\bullet}_{O}$
Reaction VI	$R_2O_3 + O_O + 2Si_{Si} \rightarrow (2R'_{Si} + V^{\bullet\bullet}_{O}) + 2SiO_2$
Solution energy VI	
Unbound defect:	$E_{sol} = 2E_{form}(R^{'}{}_{Si}) + E_{form}(V^{\bullet\bullet}_{O}) + 2E_{lattice}(SiO_2) - E_{la}$
Bound defect:	$E_{sol} = E_{form}(2R^{'}{}_{Si} + V^{\bullet\bullet}_{O}) + 2E_{lattice}(SiO_2) - E_{lattice}(R_2$

Another important aspect to be considered when dealing with aliovalent dopants is Coulombic attraction between different constituents of the defect itself, the substitutional doping ion and the charge compensation defects involved. In a real crystalline system this often led to the charge compensating defect being located close to the doping ion forming a bound defect. However, this effect will happen only if the energy gained via the Coulombic attraction overcomes the energetic costs due to the distortions in the lattice, that is usually higher when a number of defects are close together. One possible way to deal with this effect is to consider the defect as a whole, including the dopant ions and the charging compensation defects, and calculating the formation and solution energies for the bound defect. The difference between the formation energy of the bound defect with the sum of the formation energy of the constituents forming the defect (unbound defect) will give the binding energy and if the energy of the bound defect is lower this will be an indication that the bond configuration is more stable and it will be more likely to be found in the matrix.

In the present work both bound and unbound defects were considered, and their corresponding energetic balance equations are also shown in table 1. Since different mechanisms of incorporating the dopant in the matrix involve different numbers of individual defects, for comparison purposes the final values were normalized by the number of basic units forming the defect cluster itself. As an example, take the first mechanism in Table 1, incorporation of the trivalent dopant ion at the Cd site compensated by Cd vacancy. There are 3 basic units in this defect, 2 dopants sitting at Cd sites and one Cd vacancy. So, both the unbound and the bound solution energies calculated via the corresponding energetic balance equations were divided by 3.

Another issue to be considered is how far the basic defects composing a specific defect would be to be considered as a bound defect. The simple answer would be: this

should be tested and in the present work, the maximum distance of around 15 Å among basic units was chosen since this is the cut-off distance for the short-range interaction potential terms.

RESULTS AND DISCUSSIONS

The cadmium silicates crystalline structures considered in the present work have more than one symmetrically non-equivalent site for Cd, Si and O. In the $CdSiO_3$ matrix there are three symmetrically non-equivalent sites for the silicon and cadmium ions, and nine for the oxygen ion (see Figure 1 A)). Cd_3SiO_5 has two symmetrically non-equivalent sites for the cadmium and oxygen ions and only one site for silicon (see Figure 1 C)), while there is only one symmetrically non-equivalent site for each kind of ion in the Cd_2SiO_4 matrix (see Figure 1 B)). Any defect modelling strategy have to take these into consideration to produce meaningful energetic values that could be used for predicting the most likely defect type. Due to these diverse set of non -equivalent sites, cadmium silicate matrices yield a wide number of combinations for the reactions described in Table 1 resulting in a wide number of solution energies for each defect.

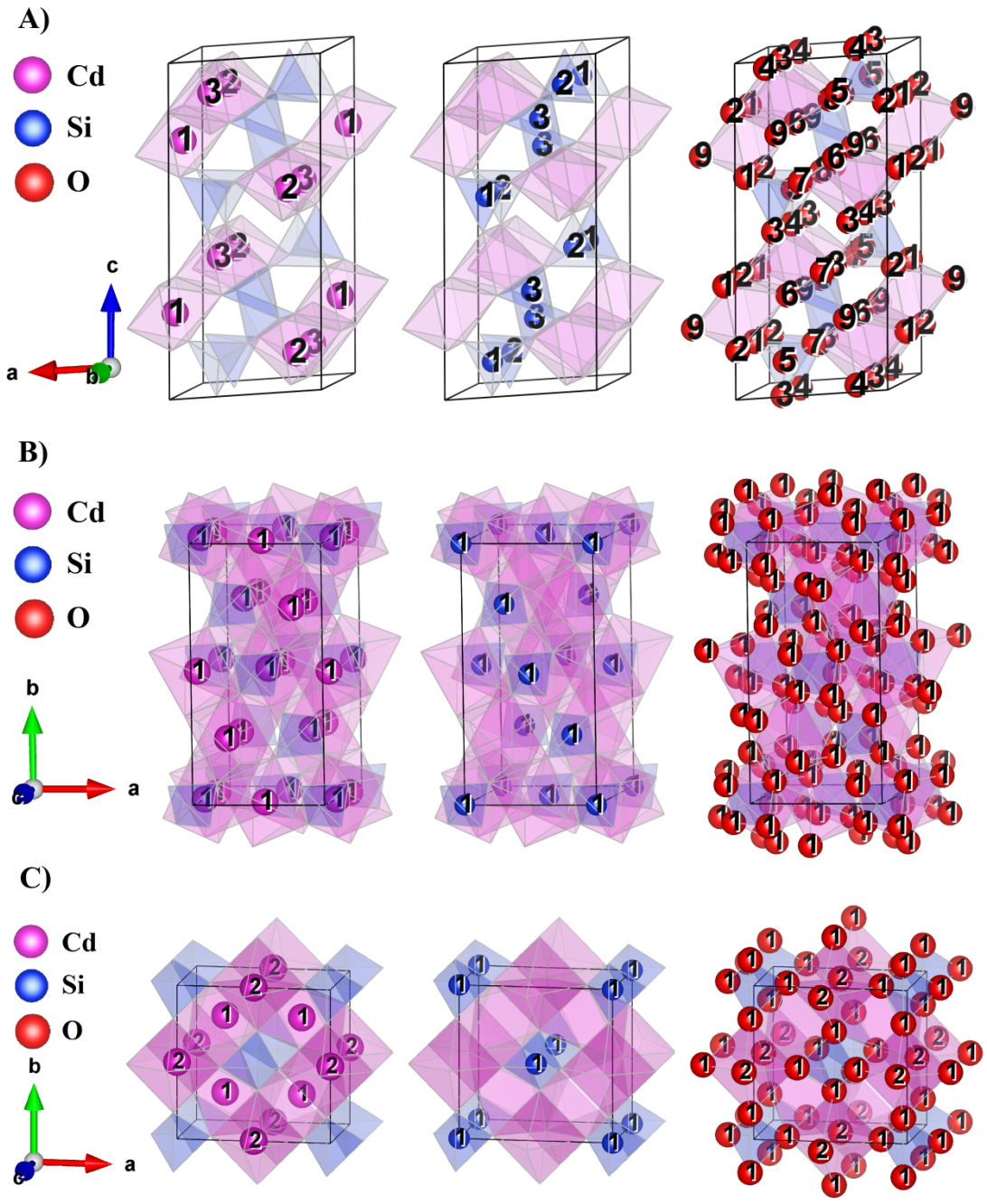

Figure 1: Identification of the symmetrically non-equivalent sites A) for the $CdSiO_3$ matrix, with three symmetrically non-equivalent sites for cadmium and silicon ions and nine for oxygen ions, B) for the Cd_2SiO_4 matrix, showing only one symmetrically non-equivalent sites for cadmium, silicon and oxygen ions, and C) for the Cd_3SiO_5 matrix, with two symmetrically non-equivalent sites for cadmium and oxygen ions and one for silicon ions.

Figure 2 describes the behaviour of the solution energy of defects in $CdSiO_3$ host for each of the doping ions for all possible combinations in all reactions covered in the present work. Each defect/reaction shown in Table 1 is represented by a symbol/colour and the spreading of them indicates the variation in the solution energy considering all possible combination of sites for each defect model.

It can be observed that defects with R at the cadmium site are more favourable than those defects whose dopants are at Si sites. Furthermore, reaction I, associated to the formation of the $2R_{Cd}^{\bullet} + V''_{Cd}$ defect, is the most favourable doping mechanism for all dopants at both temperatures, 0 and 300 K.

Such results can be explained if we carefully look the variation between ionic radii of the dopants and substitutional ions. The trivalent rare earth family presents an ionic radii range from 86.1 pm (Lu^{3+}) up to 102.0 pm (Ce^{3+}) for coordination number 6. As a rule, the substitution of one host element by one dopant is favoured by a combination of factors: ionic radius of host element, similarity of charge and coordination number of substitutional site. From the point of view of the charge similarity, all reaction in Table 1 show trivalent dopants at substitutional sites with different charges which require charge compensation mechanisms to keep the crystal neutral. Therefore, it is natural to assume that charge similarity is not the determining factor for dopant substitutional choice. The ionic radii of the dopant ions are closer to the Cd (95 pm, CN:6) than the Si(26 pm, CN:4) ions and this induces a natural choice of the dopant to choose the Cd sites. Moreover, the Cd sites have an average distance between Cd and its first neighbors around 2.34 Å while the distances from the Si ions to their first neighbors are around 1.62 Å. All these effects contributed for preference of the trivalent rare earth ions to substitute at one of the Cd sites.

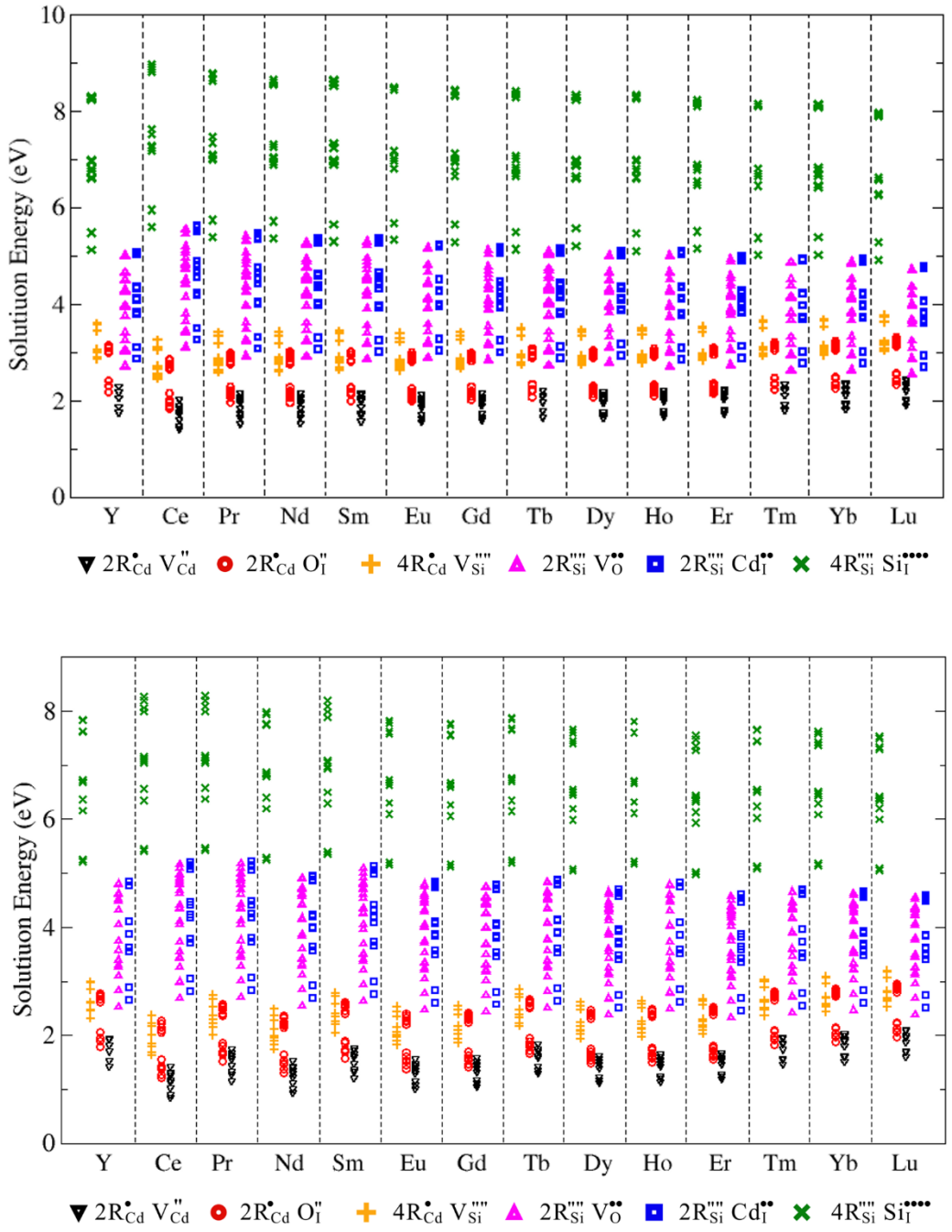

Figure 2: Solution energy graph for the different solution equations for 3^{+} doping ions in the $CdSiO_3$ matrix at 0 K and 300 K, respectively.

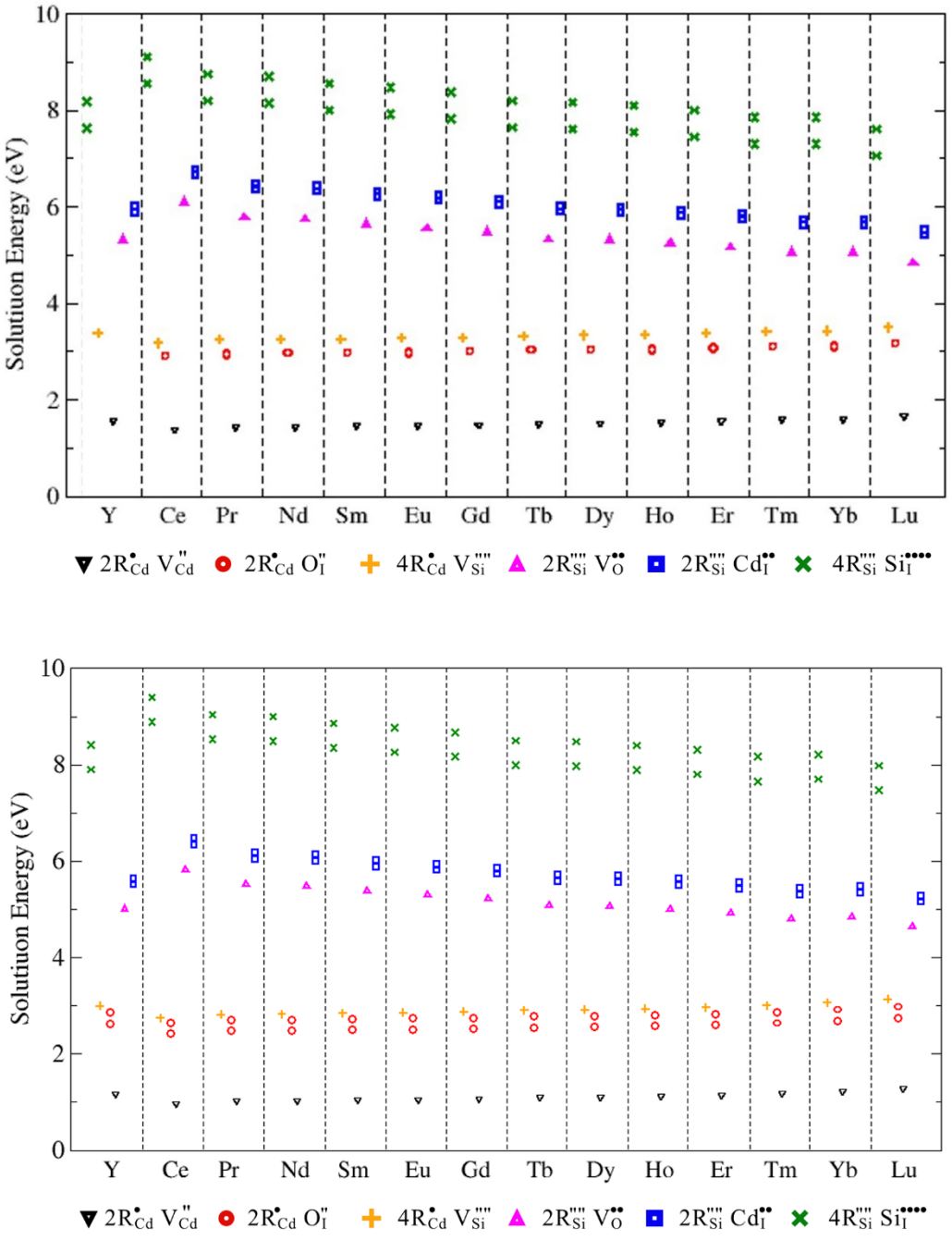

Figure 3: Solution energy graph for the different solution equations for 3^{+} doping ions in the Cd_2SiO_4 matrix at 0 K and 300 K, respectively.

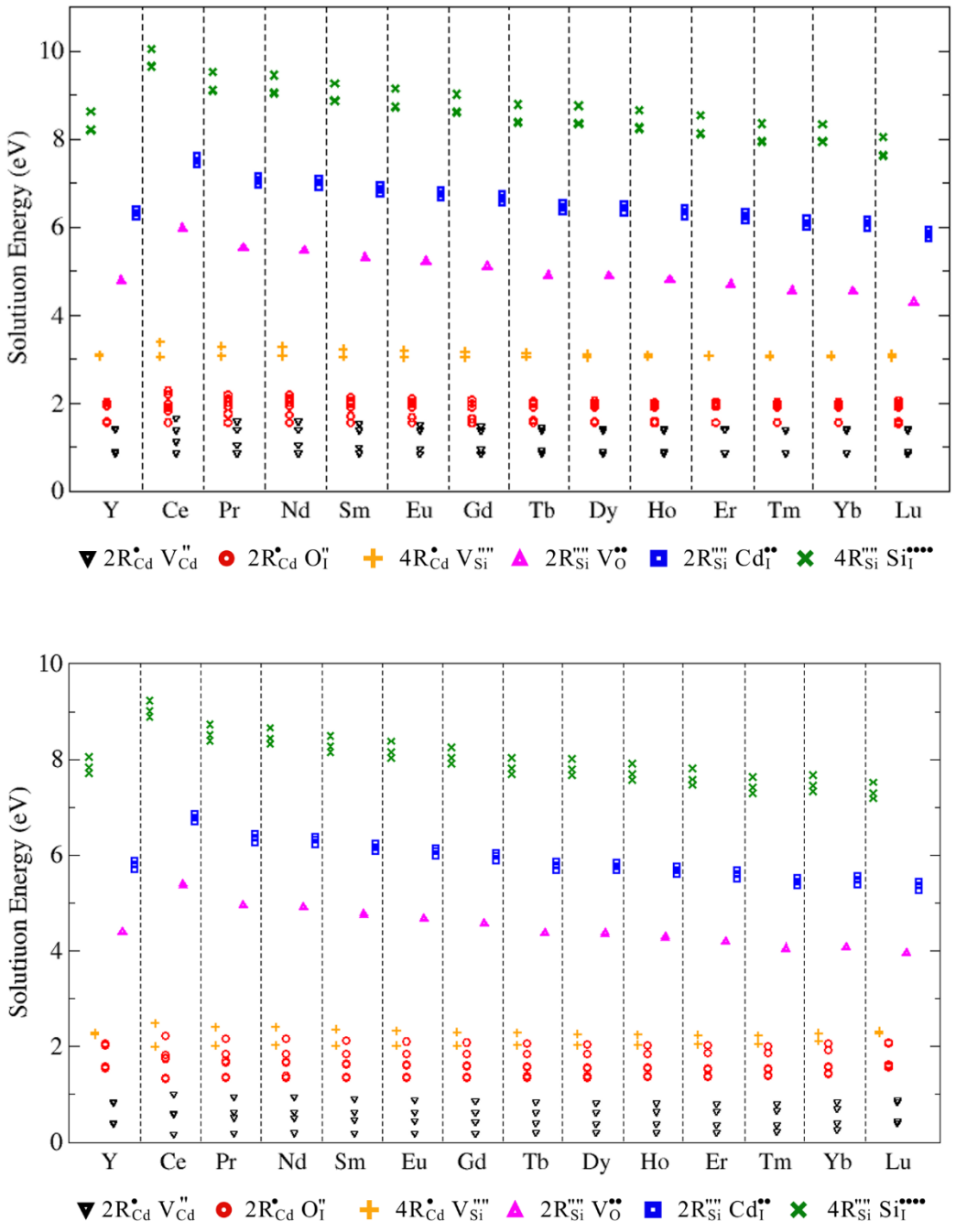

Figure 4: Solution energy graph for the different solution equations for 3^{+} doping ions in the Cd_3SiO_5 matrix at 0 K and 300 K, respectively.

Figures 3 and 4 show results for the other 2 Cd-silicates phases considered in this work. As expected, doping in Cd site is the most favourable extrinsic defects also in these structures. Results also shown that the compensation defect for all R ions in all Cd-

silicate structures is the Cd-vacancy. Such compensation can be related with ease of creation of CdO pseudo-Schottky defect in pure structures as argued in reference [16].

Experimental reports have assigned two possible compensation mechanism for $CdSiO_3$ structure: interstitial oxide ion and Cd-vacancy [12,31]. We can extend this possibility for other cadmium silicate structures taking account results presented in Figures 3 and 4. Otherwise, the hypothesis of interstitial oxide ion compensation due to considerable free space in $CdSiO_3$ structure[12] was not observed here and this defect type is higher in energetic costs compared with the compensation via Cd vacancy.

Up to this point, only unbound defects were considered, and that is equivalent to considering that the dopant(s) and the charge compensation defect(s) are so far apart in the matrix that no interaction among them is taken into account. As discussed earlier, this is a quite unrealistic situation mainly if the individual defects are charged, as the case for all defects considered in the present work. A more realistic situation would be considering the dopant(s) and the charge compensation defect(s) as part of a single defect, or a defect cluster, where the interactions among them are rightly incorporated in the final energetics of the defect. But, the number of possible combinations of all individual defects is quite big for the cadmium silicates due to diversity of sites and to the symmetry of the lattices. A more comprehensive approach is to use the energy values obtained for the unbound defects, choose only the few lowest energetic defect configurations, and reanalyse them in the defect cluster approach. In the present work, only the two defects with lowest unbound solution energies were considered in order to reduce the number of possibilities and to make the calculations more feasible. Also, the bound defect calculations were done only for the $CdSiO_3$ matrix due to two main reasons: i- among the cadmium silicate hosts, $CdSiO_3$ is far the most studied one due to the diversity of its luminescence properties, however key aspects of the luminescence mechanisms are still not fully understood, and

ii-) connected to the previous one, the final configurations of the defects generated due to doping in the CdSiO3 matrix can give important insights to understand the characteristic of absorption and emission of light giving additional details useful for the models of the optical properties of the material. The two unbound defects that were considered hereafter and that have the lowest solutions energies are listed in Table 2. Similar to the unbound defects, the bound extrinsic defects were calculated at 0 K and 300 K for the two configurations with lowest energies listed in table 2, and it is worth reinforcing here that the calculations of the free energies were done within the limits of the harmonic approximation. As previously discussed, due to the large number of symmetrically non-equivalent sites in the $CdSiO_3$ matrix, it is important to calculate the bound solution energy considering as much combinations of the lattice sites occupied by the basic defect composing the bound defect as it is possible. .

Table 2: Reactions used for calculating bound extrinsic defects.

	0 K and 300 K
Lower energy	$R_{Cd(2)}^{\bullet} + R_{Cd(2)}^{\bullet} + V_{Cd(1)}^{''}$
2nd lowest energy	$R_{Cd(2)}^{\bullet} + R_{Cd(2)}^{\bullet} + O(1)_{I}^{''}$

Table 3 presents all the distances between the three basic defects (2 $R_{Cd(2)}^{\bullet}$ and 1 $V_{Cd(1)}^{''}$) and the $R_{Cd(2)}^{\bullet} - V_{Cd(1)}^{''} - R_{Cd(2)}^{\bullet}$ angles (with the $V_{Cd}^{''}$ in the vertices), for eleven different configurations (identified in Roman numbers) obtained by arranging the 3 basic defects in nearby lattice sites in the $CdSiO_3$ matrix. These configurations represent all possibilities for arranging the basic defects within a maximum distance smaller than 15Å, and this means a longest distance within 1-2 lattice parameters, depending on the crystallographic axis taken as reference. .

Table 3: Angles and Distances between the constituents of the bound $R_{Cd(2)}^{\bullet} - R_{Cd(2)}^{\bullet} - V_{Cd(1)}^{''}$ defects in the $CdSiO_3$ matrix for ten different arrangements of the three basic defects, 2 $R_{Cd(2)}^{\bullet}$ and 1 $V_{Cd(1)}^{''}$. The angle is taken with the cadmium vacancy at the vertices All values quoted here are related to the initial positions of the 3 basic defects, i.e., before the energy minimisation accompanied by the lattice relaxation induced by the defects.

Configuration	I	II	III	IV	V	VI	VII	VIII	IX	X	XI
Angle (°)	12.79	24.13	42.04	55.68	61.91	71.91	99.73	112.74	148.78	169.91	177.63
Dist. R_1-R_2 (Å)	7.20	9.97	7.20	11.61	7.20	7.20	12.44	12.44	10.81	11.99	6.97
Dist. R_1-V (Å)	3.43	14.92	6.52	13.55	6.16	6.49	11.34	3.43	3.54	3.43	3.43
Dist. R_2-V (Å)	10.51	5.73	10.57	10.71	7.62	5.73	3.54	10.71	7.62	8.6	3.54

Figure 5 shows the representation of two configurations used in the calculations of the $2R_{Cd(2)}^{\bullet} - V_{Cd(1)}^{''}$bound defects. Figure 5 a) shows the configuration I, as in table 3, that has a very acute V-shape with the smallest possible angle, allowed by the crystalline structure of CdSiO3. This configuration has the two dopants almost aligned with short distance between them of about 7.2Å. Figure 5 b) shows the configuration XI, as for in table 3, with the largest angle formed between the defects, of approximately 177.6º, where

the two dopants and the Cd vacancy is almost in a straight line with the vacancy almost in the middle point of the line connecting the two dopant ions. It is shown later in the paper that the angular position is of great importance for the value of the energy of the defects, with the angle being more relevant than the distances between the dopant ions.

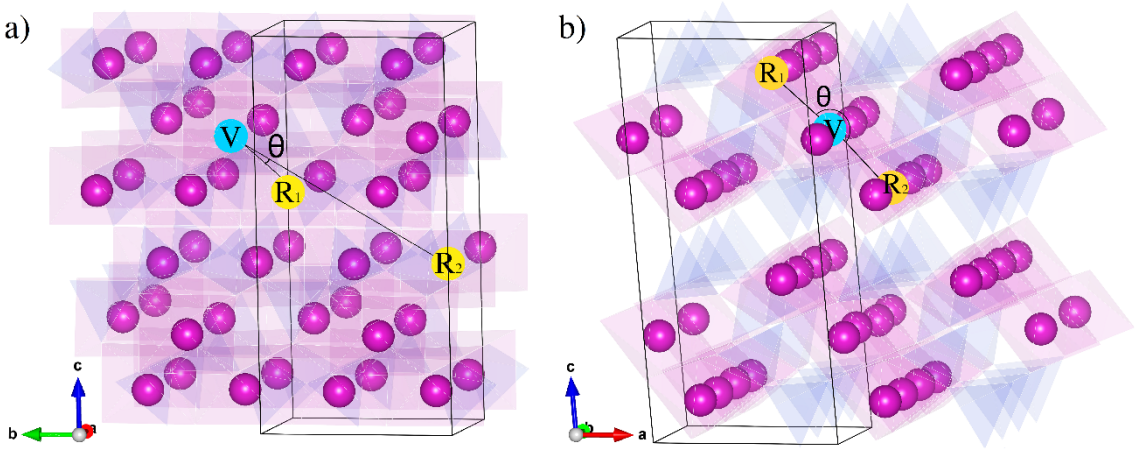

Figure 5: Example of configurations for the calculations of the bound extrinsic defects. The yellow balls represent the two Cd sites that are replaced by the dopant ions and in blue, it is shown the Cd site where the vacancy is located. a) Representation of the configuration I (see table 3) of the two dopants and the vacancy in the vertices in a V-shape configuration with the smallest possible angle allowed by the CdSiO3 crystal structure. b) shows the configurations XI (see table 3) with the two dopants and the Cd vacancy in an almost strait line configuration. This ended up being the most favourable configuration for doping with rare earth trivalent ions, as commented in the text.

Although the bound $2R_{Cd(2)}^{\bullet} - V_{Cd(1)}^{''}$ defects are the ones with the lowest solution energies in all cases, as it will be shown later, for the sake of clarity, it is important to draw a few lines about the second defect type that was considered in the calculations of the bound defects, named, the $2R_{Cd(2)}^{\bullet} - O(1)_{I}^{''}$ type defects. The general idea is the same

as it was done for the $2R_{Cd(2)}^{\bullet} - V_{Cd(1)}^{''}$ defect. A few $CdSiO_3$ unit cells were drawn around the origin and the $O(1)_I^{''}$ defect is positioned as close as possible to the origin. If it was necessary, the origin (and all positions of the ions) is shifted so the interstitial site is right in the origin. After that, all Cd(2) sites, that have to accommodate 2 dopant ions, are marked and all possible configurations of arranging the two dopants are registered. After that the subset of such configurations that has the longest distance between the basic defects smaller than a maximum distance of about 15Å are collected and simulated to obtain all solution energies for the different configurations of the $2R_{Cd(2)}^{\bullet} - O(1)_I^{''}$ defects. There were 11 of such configurations for $2Tr^{\circ}_{Cd(2)} + V''_{Cd(1)}$ with the distances and angles are in the table A1 of the Appendix and 28 of such configurations for $2R^{\circ}_{Cd(2)} + O''_{I(1)}$ with the distances and angles are in the table A2 of the Appendix.

The results of the solution energies for all configurations and for the two types of defects are shown in figures 6. The computed values of the bound solution energies are tabulated in the table A3 of the appendix, for the sake of comparison.

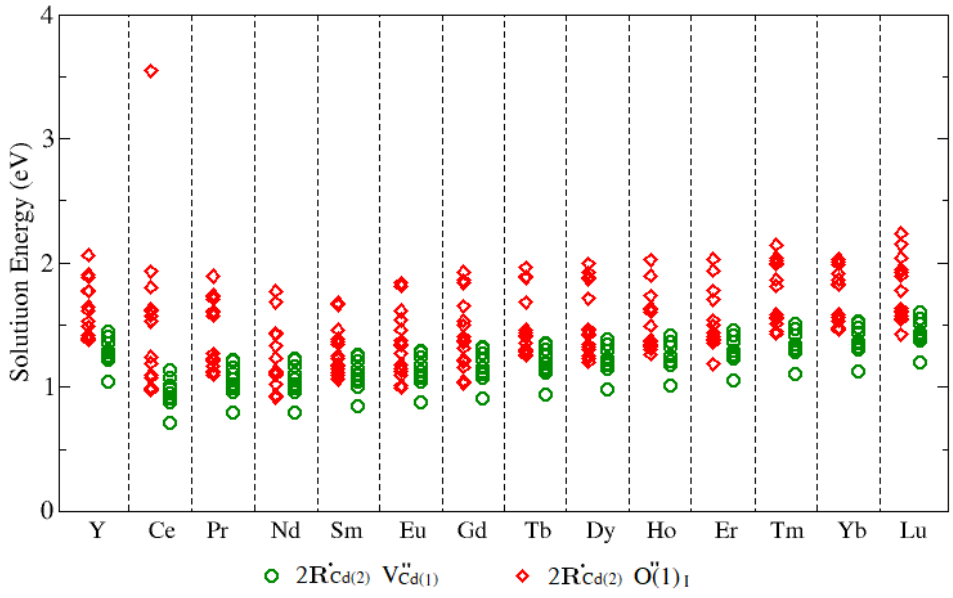

(a)

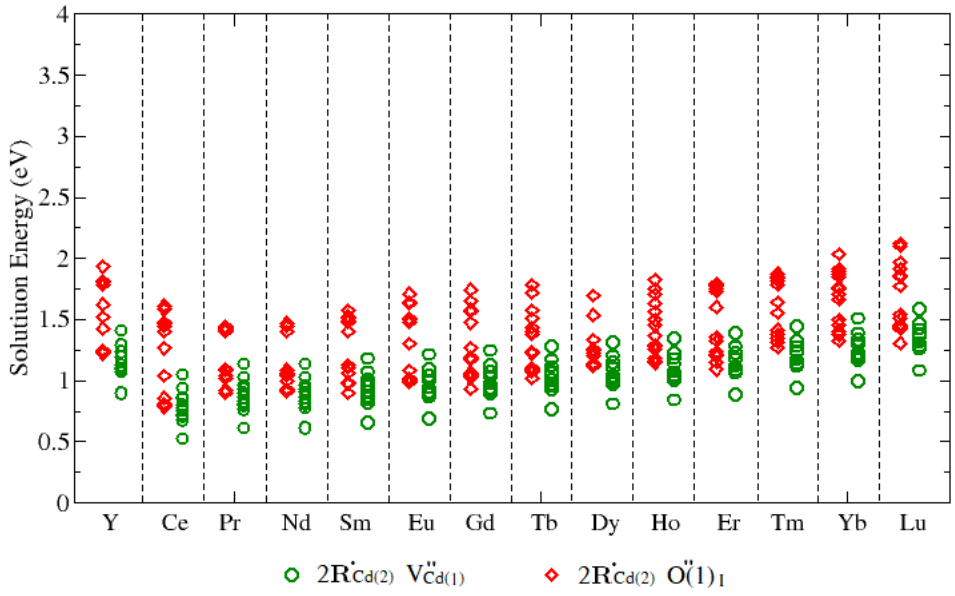

(b)

Figure 6: Normalized solution energy for the bound defects in the $CdSiO_3$ matrix. Plot of the first and second lowest solution energies a) at 0 K (aa) and at 300K (b).

The graph in Figure a) shows the behaviour of the solution energy of the bound defects calculated at 0 K. and the graph in Figure b), the solution energies obtained at 300K are presented. The solution energies presented here are normalised to the number of basic defects contained in the bound defect, that is 3 in both $2R_{Cd(2)}^{\bullet} - V_{Cd(1)}^{''}$ and 2 $R_{Cd(2)}^{\bullet} - V_{Cd(1)}^{''}$ cases. The results shown in figures 6 clearly pointed out once again that the defect type giving the lowest solution energies for all dopants are the $2R_{Cd(2)}^{\bullet} - V_{Cd(1)}^{''}$ ones, with doping ions replacing 2 Cd(2) charge-compensated by Cd vacancy created in Cd(1) site, a similar conclusion drawn from the calculations shown previously for the unbound defects. .

At this point we may argue that there was no significant gain in wasting a lot of time investigating the bound defects if the general conclusions are the same as for the unbound defects that are much easier to obtain and much less time consuming. But it should be noticed that with the bound and unbound defects being calculated a lot of new information is now readily available that are quite useful to understand the behaviour of some interesting optical properties of such materials.

Firstly, upon comparing figure 6 with figure 2, it is possible to conclude that the binding energy plays a quite important role dropping the solution energies from around 2eV to around 1eV per constituent of the defect. This means a reduction of 50% of the total energetic costs to create a $2R_{Cd^{\bullet}(2)} - V_{Cd^{''}(1)}$ defect in the $CdSiO_3$ matrix, a quite significant reduction in terms of energetic balances.

Another interesting issue is that the energetic cost for that defect slightly but steadily increased as the ionic radius of the rare earth ion decreased or, the atomic number increased. As already mentioned earlier, the ionic radii range from 86.1 pm, for Lu^{3+}, up to 102.0pm, for Ce^{3+}, in 6-fold coordination. Cd^{2+} also in 6-fold coordination, presents an ionic radius of about 95pm, with size right in the middle of the family of the trivalent rare earth ions. So, from the point of view of ionic size alone, one may expect that both extremes, Lu3+ and Ce3+, would require higher energies since the lattice would be more distorted to accommodate bigger differences in sizes. The charge difference cannot also explain that, since all rare earth considered here have the same charges. So, this behaviour of increasing energetic costs on moving along the rare earth series, from the bigger to the smaller one, has to be connected to something else particular to the rare earth series itself. Upon inspecting the solution energies of the unbound defects, presented in figure 3, it can be seen that this feature is also presented in the results for 0K but in a more subtle way,

while for the results of the unbound defect energies at 300K it is not clear if the energetic costs steadily increased as the dopant ionic decreased. So, it seems to be a feature that depends on the binding of the defect and the role of the particular rare earth ion in it.

Thirdly, and possibly a more interesting result concerning the understanding of the optical properties of doped CdSiO3, is that the final configuration of the defects and the final position of the surrounding neighbouring ions of the dopants is readily available allowing the analysis of the possible symmetry experienced by the dopants in the $CdSiO_3$ matrix. So, it was worth spending time to carefully analyse all possible configurations for the bound defects. In this scenario, the results in figure 6 indicates that the configuration XI for the $2R_{Cd(2)}^{\bullet} - V_{Cd(1)}^{''}$ is the one that gave the lowest solution energies for all trivalent rare earth ions.

One of the important aspects that influences the optical properties of the trivalent rare earth ions is the site symmetry where they are located in the matrix. So, this is of key importance to understand the luminescence characteristics that are generated when trivalent rare earth ions enter as dopants in the $CadSiO_3$ matrix.

The geometric configuration of the surrounding neighbourhood of the dopant can be easily obtained from the relaxed lattice positions for the bound defect calculations. Figure 6 a) shows the relaxed lattice in the region close to the 2 dopant ions for the $2R_{Cd(2)}^{\bullet} - V_{Cd(1)}^{''}$ bound defect in configuration XI, taking as an example the case of R=Lu3+. Similar pictures can be drawn for all other rare earths. Figure 6b shows the two polyhedra related to the two Lu3+ dopants. In this latter figure is also shown the notation for the distances and angles that were analysed to understand the site symmetry surrounding the dopants. The six distances, polyhedra volume and four angles was collected for all

dopants and they are shown in figure 7, 8 and 9, respectively, potted as a function of trivalent rare earth ionic radii.

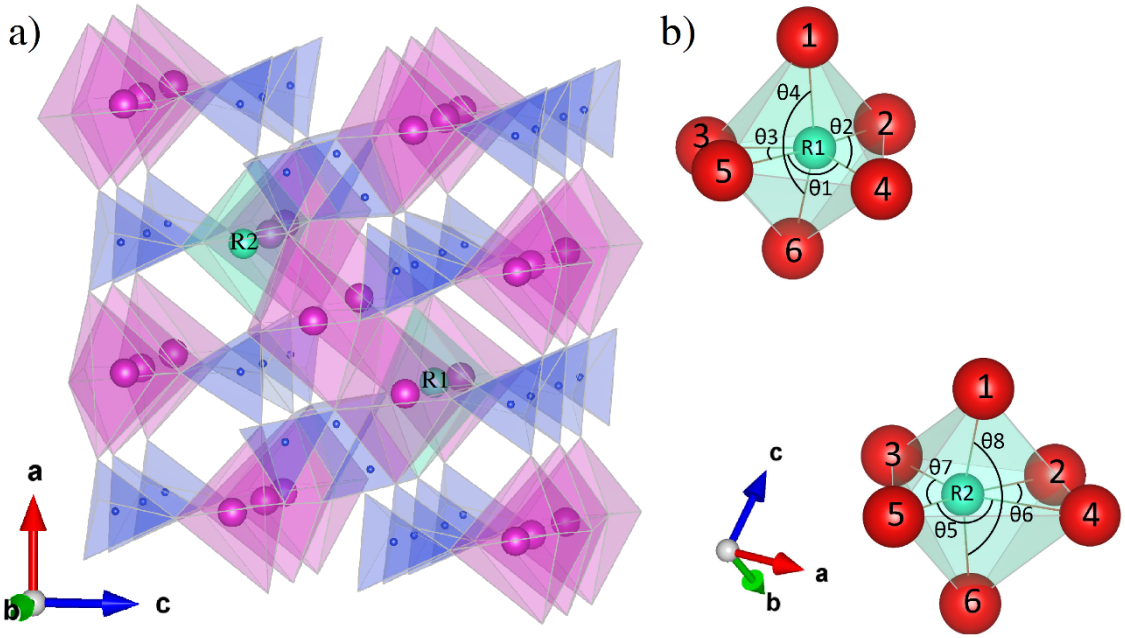

Figure 6: In a) we have the lowest energy configuration for doping optimized for all R analysed. In b) we have a description of the numbering of the ions and angles analysed.

In general, we can observe that doping only generates light deformations and maintains polyhedra volume and bond lengths very close to the reference (Cd polyhedrons). To better analyse these deformations, we will calculate distances between the ions, some crucial angles for the formation of the polyhedron and the volume of the polyhedra for the two extremes of values for the ionic radii of the doping ions that are Lu and Ce. The indication of the placement of the ions and the related angles are shown in Figure 6 b).

In figure 7 we have the results for the bond lengths between R - O for the two polyhedra of R that form the most energetically favourable defect, in order of ionic radii. In red we have the reference values for the original Cd polyhedron (to facilitate the visualisation we have the area in gray). The larger the ionic radius of the dopant ion, the longer the bond lengths between R - O. Note that for each dopant ion we have 12 bond lengths, 6 for each doped polyhedron.

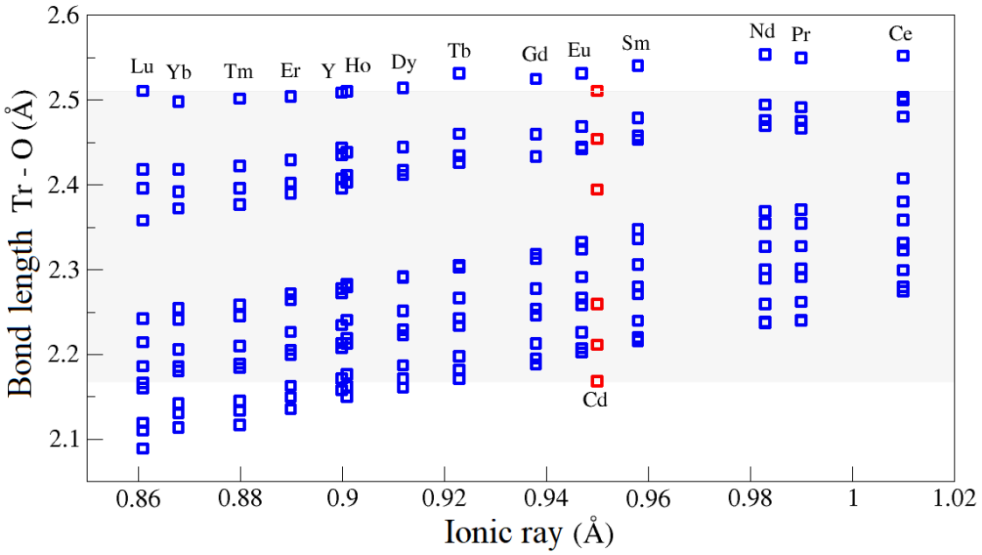

Figure 7: Bond length between R^{3+} - O ions for the relaxed lattice around the two dopants for the $2R_{Cd^{\bullet}(2)} - V_{Cd^{''}(1)}$ bound defect, configuration XI. The site identification, site R1 and site R2, are given in figure 6b.

From the graph in Figure 8, we can see that the volumes of the polyhedra increase according to the size of the ionic radii of the dopants. There is always a polyhedron that reduces in volume in relation to the other. The Eu polyhedron has a volume closer to the Cd original.

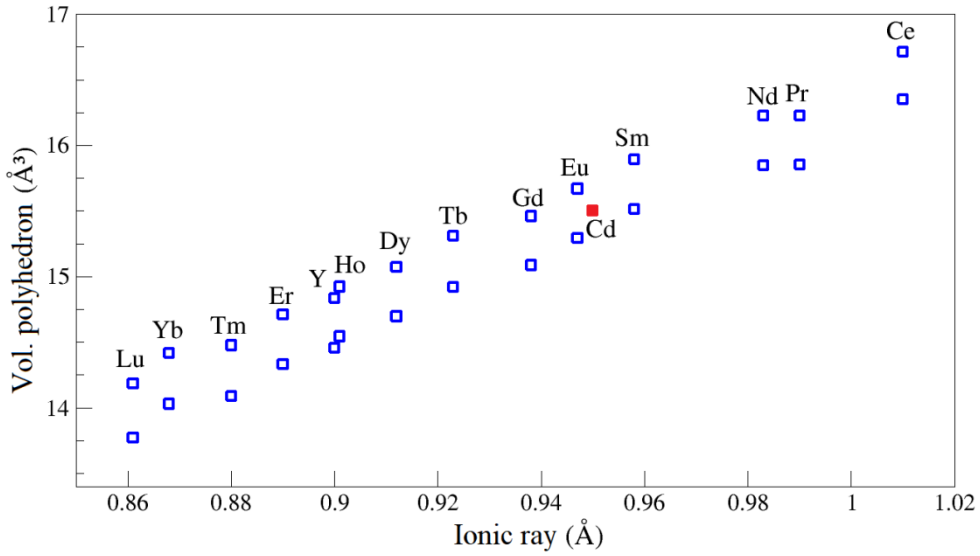

Figure 8: Volume of the polyhedra of the R^{3+} - O ions for the relaxed lattice around the two dopants for the $2R_{Cd(2)}^{\bullet} - V_{Cd(1)}^{''}$ bound defect, configuration XI. The site identification, site R1 and site R2, are given in figure 6b.

The graph in Figure 9 shows the results for the angles analysed. The following interesting features can be drawn from figures 9: i- none of the polyhedra angles showed appreciable changes as moving along the rare earth series compared to the original angles of Cd polyhedra; ii- angles θ2, θ5 and θ7 are larger when doped, while all others are slightly smaller, probably caused by the vacancy in the region between the polyhedra.

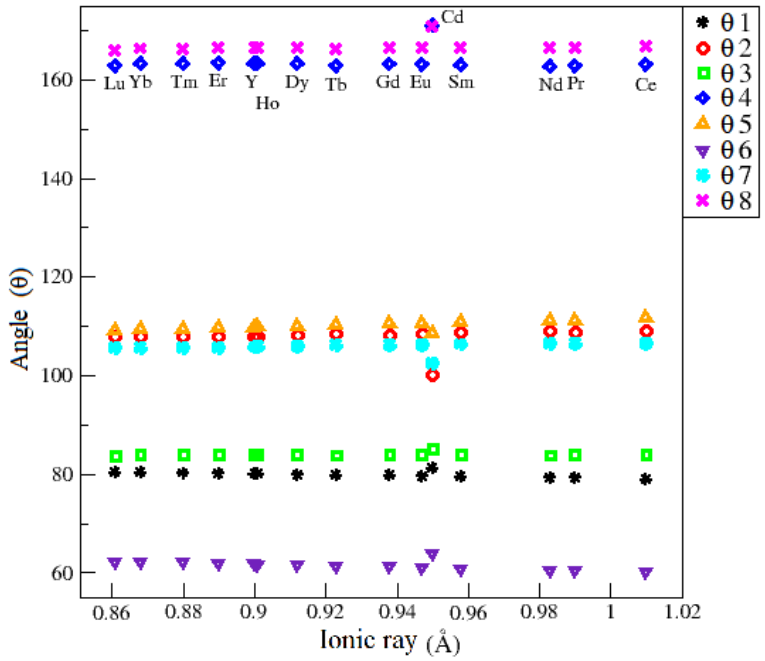

Figure 9: Angles analysed in the polyhedra of the R^{3+} - O ions for the relaxed lattice around the two dopants for the $2R_{Cd(2)}^{\bullet} - V_{Cd(1)}^{''}$ bound defect, configuration XI. The site identification, site R1 and site R2, are given in figure 6b.

In Figures 10 and 11 we have a qualitative approach to the distortions caused by substitutional doping made at Cd sites for Ce and Lu respectively. Figure 10 shows how the Ce polyhedra were after the relaxation of the lattice, compared to the relaxation of the Cd lattice, in black dotted circles. In Figure 10 a) we have an overview of the two doped polyhedra, we see from this angle that the biggest distortions are in the positions of the Ce ions. in Figure 10 b), c) and d) we have the views in the yz, xz and xy planes respectively. Figure 11 shows the Lu polyhedra after the relaxation of the defective lattice, remembering that the Lu ion has a smaller ionic radius than the Cd ion. With this in mind, we can see (in Figure 11 a)) a distancing of the Lu polyhedra because of the repulsion between the two Lu ions, as can also be seen in the xy plane (Figure 11 d)). In addition, we also observe the reduction of bond lengths between oxygen and lutetium ions, mainly in Figures 11 b) and 11 c).

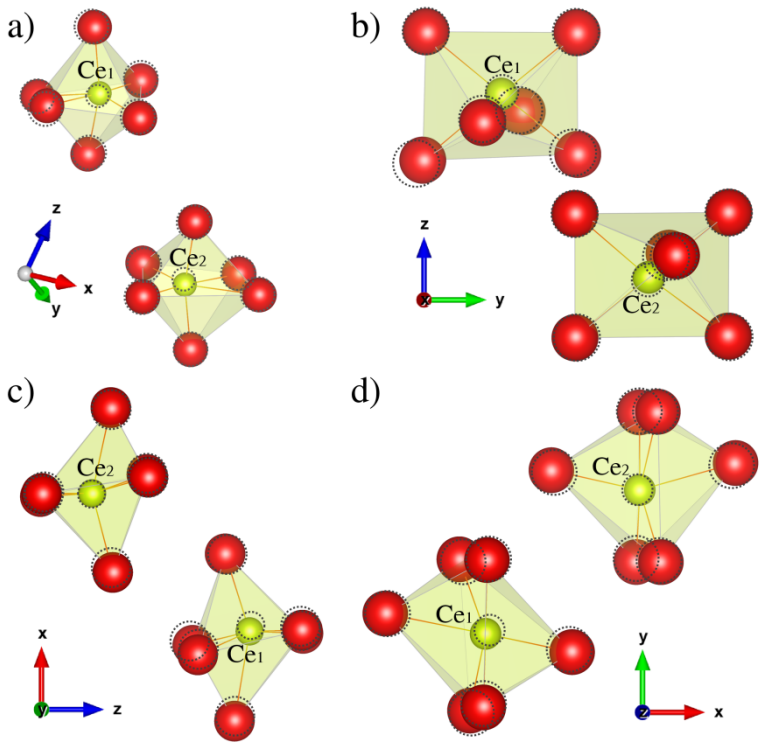

Figure 10: Polyhedra of Ce after relaxation of the network, in the dotted circles in black we have the representation of the position for the original ions of Cd and O. In a) we have an overview of the two doped polyhedra, in b) we have the view in the YZ plane, in c) we have the view in the XZ plane and in d) we have the view in the XY plane.

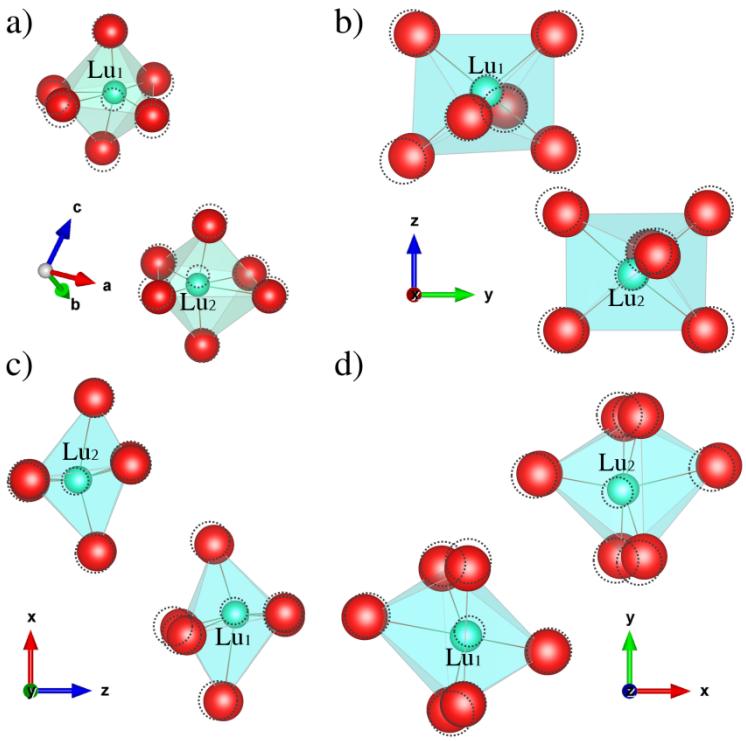

Figure 11: Polyhedra of Lu after relaxation of the network, in the dotted circles in black we have the representation of the position for the original ions of Cd and O. In a) we have an overview of the two doped polyhedra, in b) we have the view in the YZ plane, in c) we have the view in the XZ plane and in d) we have the view in the XY plane.

Looking at

Table , we can see some trends. The first trend that we will highlight is the decrease in the values of the solution energy at 300 K when compared to 0 K. This is because the thermal energy supplied to the lattice helps to minimize the total energy of the defect, since this energy provides a greater mobility to the ions, so we can find a minimum energy less at 300 K, than at 0 K. As the defect energy is calculated by subtracting the energy of the perfect lattice from the energy of the lattice with defect, the contribution from the thermal energy is compensated by this subtraction. Another very important trend to be mentioned, mainly for the results involving the ions of rare earth, is the relationship between the angle and the solution energy value. We can see that bound defect energy decreases when angle of three sites approaches to 180 degrees. For example, at an angle close to 12 degrees it has the lowest energy of acute angles, in this angle the three ions involved are almost aligned, the two doping in sequence with the vacancy at the tip (see Figure 6 a)). In the lower energetic case (see Figure 6 b)), there is an angle of approximately 177 degrees. We also have practically a straight line connecting the three ions with the vacancy centred between the two doping ions. This configuration forms a set of two dipoles, since the cadmium vacancy (charge -2e) is located between the doping ions (charge + 1e).

Conclusions

In this work, we analysed the trivalent rare earth doping in the cadmium silicate hosts ($CdSiO_3$, Cd_2SiO_4 and Cd_3SiO_5) through classical computer modelling. Initially, we construct reactions to calculate solution energies taking account the smaller number of basic defects in the composition. Results show that the most energetically favourable

defects are R ions occupy the cadmium site with Cd-vacancy charge compensation for all stoichiometries. These results agreed with experimental results reported in the literature.

We also analysed if there is a preferable configuration for the Cd-vacancy compensation defect in the $CdSiO_3$ structure. Therefore, we tested different arrangements of the ions involved in the formation of Cd-vacancy compensation defects in the $CdSiO_3$ matrix. Results demonstrated that for rare earth ions there is a preferred arrangement with a distance of around 7 Å and angle closer to 180º. The distance represents the second coordination sphere such as happened in the case of intrinsic defects. There is the possibility of a set of two dipoles caused by charge balance because the Cd-vacancy defect is in the middle of two R ions.

Acknowledgments

The authors are grateful to the Federal University of Sergipe (UFS), to the LPCM group, to the funding agency CAPES, to the CENAPAD-SP and to the CENAPAD-UFC.

REFERENCES

[1] B. Lei, Y. Liu, Z. Ye, C. Shi, Luminescence properties of CdSiO3:Mn2+ phosphor, J. Lumin. 109 (2004) 215–219. https://doi.org/10.1016/j.jlumin.2004.02.010.

[2] S.K. Singh, Red and near infrared persistent luminescence nano-probes for bioimaging and targeting applications, RSC Adv. 4 (2014) 58674–58698. https://doi.org/10.1039/c4ra08847f.

[3] A. Jain, A. Kumar, S.J. Dhoble, D.R. Peshwe, Persistent luminescence: An insight, Renew. Sustain. Energy Rev. 65 (2016) 135–153. https://doi.org/10.1016/j.rser.2016.06.081.

[4] B.M. Manohara, H. Nagabhushana, K. Thyagarajan, S.C. Prashantha, B.M. Nagabhushana, C. Shivakumara, S.C. Sharma, Self-propagating combustion synthesis of CdSiO3 nano powder: Structural and dosimetric applications, Mater. Res. Express. 2 (2015) 25005. https://doi.org/10.1088/2053-1591/2/2/025005.

[5] K. Van den Eeckhout, P.F. Smet, D. Poelman, Persistent Luminescence in Eu2+-Doped Compounds: A Review, Materials (Basel). 3 (2010) 2536–2566. https://doi.org/10.3390/ma3042536.

[6] T. Aitasalo, J. Hölsä, H. Jungner, M. Lastusaari, J. Niittykoski, Thermoluminescence Study of Persistent Luminescence Materials: Eu 2+ - and R 3+ -Doped Calcium Aluminates, CaAl 2 O 4 :Eu 2+ ,R 3+, J. Phys. Chem. B. 110 (2006) 4589–4598. https://doi.org/10.1021/jp057185m.

[7] J. Xu, S. Tanabe, Persistent luminescence instead of phosphorescence: History, mechanism, and perspective, J. Lumin. 205 (2019) 581–620. https://doi.org/10.1016/j.jlumin.2018.09.047.

[8] P.F. Smet, I. Moreels, Z. Hens, D. Poelman, Luminescence in sulfides: A rich history and a bright future, Materials (Basel). 3 (2010) 2834–2883. https://doi.org/10.3390/ma3042834.

[9] T. Matsuzawa, Y. Aoki, N. Takeuchi, Y. Murayama, A New Long Phosphorescent Phosphor with High Brightness, SrAl2 O 4 : Eu2 + , Dy3 + , J. Electrochem. Soc. 143 (1996) 2670–2673. https://doi.org/10.1149/1.1837067.

[10] C.M. Abreu, R.S. Silva, M.E.G. Valerio, Z.S. Macedo, Color-control of the persistent luminescence of cadmium silicate doped with transition metals, J. Solid State Chem. 200 (2013) 54–59. https://doi.org/10.1016/j.jssc.2012.11.031.

[11] Y. V. Kuznetsova, A.A. Rempel, M. Meyer, V. Pipich, S. Gerth, A. Magerl, Small angle X-ray and neutron scattering on cadmium sulfide nanoparticles in silicate glass, J. Cryst. Growth. 447 (2016) 13–17. https://doi.org/10.1016/j.jcrysgro.2016.04.058.

[12] L.C.V. Rodrigues, J. Hölsä, M. Lastusaari, M.C.F.C. Felinto, H.F. Brito, Defect to R3+ energy transfer: Colour tuning of persistent luminescence in CdSiO3, J. Mater. Chem. C. 2 (2014) 1612–1618. https://doi.org/10.1039/c3tc31995d.

[13] M. Weil, Parawollastonite-type Cd3[Si3O9], Acta Crystallogr. Sect. E Struct. Reports Online. 61 (2006) 102–104. https://doi.org/10.1107/S1600536805015278.

[14] L.S.D. Glasser, F.P. Glasser, The Preparation and Crystal Data of the Cadmium Silicates CdSiO3, Cd2SiO4, and Cd3SiO5, Inorg. Chem. 3 (1964) 1228–1230. https://doi.org/10.1021/ic50019a005.

[15] D.F. Farias, C.M. de Abreu, S.M. V. Novais, Z.S. Macedo, Tailoring luminescent colour and life persistence of undoped CdSiO3, J. Lumin. 194 (2018) 535–541. https://doi.org/10.1016/j.jlumin.2017.10.082.

[16] E.B.V. Freire, A.L. de S. Santos, G.F. da C. Bispo, M. de A. Gomes, Z.S. Macedo, R.A. Jackson, M.E.G. Valerio, Intrinsic defects and non-stoichiometry in undoped cadmium silicate hosts, J. Alloys Compd. (2020). https://doi.org/10.1016/j.jallcom.2020.157580.

[17] Y. Liu, J. Kuang, B. Lei, C. Shi, Color-control of long-lasting phosphorescence (LLP) through rare earth ion-doped cadmium metasilicate phosphors, J. Mater. Chem. 15 (2005) 4025–4031. https://doi.org/10.1039/b507774e.

[18] B. Lei, Y. Liu, J. Liu, Z. Ye, C. Shi, Pink light emitting long-lasting phosphorescence in Sm3+-doped CdSiO3, J. Solid State Chem. 177 (2004) 1333–1337. https://doi.org/10.1016/j.jssc.2003.11.006.

[19] L.C.V. Rodrigues, M. Lastusaari, H.F. Brito, M.C.F.C. Felinto, J.M. Carvalho, J. Hölsä, O.L. Malta, Persistent luminescence of cadmium silicates, Phys. Scr. 89 (2014). https://doi.org/10.1088/0031-8949/89/4/044014.

[20] R.M. Araujo, K. Lengyel, R.A. Jackson, L. Kovács, M.E.G. Valerio, A computational study of intrinsic and extrinsic defects in LiNbO 3, J. Phys. Condens. Matter. 19 (2007). https://doi.org/10.1088/0953-8984/19/4/046211.

[21] G.F.C. da Bispo, R.A. Jackson, M.E.G. Valerio, Modelling of intrinsic defects in CaYAl3O7, Acta Phys. Pol. A. 133 (2018) 781–784. https://doi.org/10.12693/APhysPolA.133.781.

[22] G.F. d. C. Bispo, R.A. Jackson, Z.S. Macedo, M.E.G. Valerio, Ln3+ doping in CaYAl3O7 and luminescence concentration quenching studied via a new computer modelling strategy, Opt. Mater. (Amst). 92 (2019) 212–216. https://doi.org/10.1016/j.optmat.2019.04.036.

[23] M.V. do. S. Rezende, C.W.A. Paschoal, M.E.G. Valerio, R.A. Jackson, Computer modelling of Bi12SiO20 and Bi4Si3O12: Intrinsic defects and rare earth ion incorporation, J. Solid State Chem. 292 (2020). https://doi.org/10.1016/j.jssc.2020.121608.

[24] R.M. Araujo, E.F.D.S. Mattos, M.E.G. Valerio, R.A. Jackson, Computer simulation of the incorporation of V2+, V3+, V4+, V5+ and Mo3+, Mo4+, Mo5+, Mo6+ dopants in LiNBO3, Crystals. 10 (2020) 1–12. https://doi.org/10.3390/cryst10060457.

[25] A.L.D.S. Santos, E.B.V. Freire, G.F.D.C. Bispo, Z.S. Macedo, M.E.G. Valerio, Computational modelling of intrinsic defects in the orthosilicates Y2SiO5 and Lu2SiO5, J. Phys. Condens. Matter. 31 (2019). https://doi.org/10.1088/1361-648X/ab2b63.

[26] J.D. Gale, GULP: A computer program for the symmetry-adapted simulation of solids, J. Chem. Soc. Faraday Trans. 93 (1997) 629–637. https://doi.org/10.1039/a606455h.

[27] N.F. Mott, M.J. Littleton, Conduction in polar crystals. I. Electrolytic conduction in solid salts, Trans. Faraday Soc. 34 (1938) 485. https://doi.org/10.1039/tf9383400485.

[28] M.V.D.S. Rezende, D.J. Santos, R.A. Jackson, M.E.G. Valerio, Z.S. Macedo, Atomistic simulation and XAS investigation of Mn induced defects in Bi12TiO20, J. Solid State Chem. 238 (2016) 210–216. https://doi.org/10.1016/j.jssc.2016.03.029.

[29] J.D. Gale, Analytical free energy minimization of silica polymorphs, J. Phys. Chem. B. 102 (1998) 5423–5431. https://doi.org/10.1021/jp980396p.

[30] F.A. Kröger, H.J. Vink, Relations between the Concentrations of Imperfections in Crystalline Solids, Solid State Phys. - Adv. Res. Appl. 3 (1956) 307–435. https://doi.org/10.1016/S0081-1947(08)60135-6.

[31] J. Shivakumara, Chikkahanumantharayappa, R.H. Krishna, S. Ashoka, G. Nagaraju, CdSiO3:Eu3+ nanophosphor: one pot synthesis and enhancement of orange–red emission through Li+ co-doping, J. Mater. Sci. Mater. Electron. 29 (2018) 12986–12992. https://doi.org/10.1007/s10854-018-9419-z.

APPENDIX A

Table A1: Initial configuration for the bound defects of type $2R^{\circ}_{Cd(2)} + V''_{Cd(1)}$ in the $CdSiO_3$, describing distances and angle between point defects.

Config.	Angle (°)	Dist. R1-R2 (Å)	Dist.R1-V (Å)	Dist. R2-V (Å)
1	12.79	7.20	3.43	10.51
2	24.13	9.97	14.92	5.73
3	42.04	7.20	6.52	10.57
4	55.68	11.61	13.55	10.71
5	61.91	7.20	6.16	7.63
6	71.91	7.20	6.49	5.73
7	99.74	12.44	11.34	3.54
8	112.75	12.44	3.43	10.71
9	148.78	10.81	3.54	7.63
10	169.91	11.99	3.43	8.60
11	177.63	6.97	3.43	3.54

Table A2: Initial configuration for the bound defects of type $2R^{o}_{Cd(2)} + O''_{I(1)}$ in the $CdSiO_3$, describing distances and angle between point defects.

Config.	Angle (°)	Dist. R1-R2 (Å)	Dist.R1-V (Å)	Dist. R2-V (Å)
1	13.13	6.59	9.93	3.48
2	16.08	5.11	9.09	13.18
3	18.35	6.59	14.57	9.09
4	27.81	11.61	14.57	3.48
5	29.08	7.74	12.66	15.76
6	29.25	10.81	15.76	6.16
7	33.88	7.20	12.66	9.09
8	34.83	7.74	12.66	13.15
9	41.40	5.11	7.17	3.48
10	46.52	9.97	6.16	13.15
11	46.92	6.59	6.16	9.02
12	49.30	11.23	13.18	3.48
13	53.11	5.11	5.05	6.16
14	58.21	10.81	12.66	7.70
15	62.07	11.61	9.02	12.66
16	66.80	7.74	6.16	7.70
17	76.49	12.32	12.66	3.48
18	77.40	10.81	3.48	11.03
19	77.56	9.97	9.09	6.50
20	80.48	10.81	10.83	3.48
21	89.16	11.61	9.93	6.16
22	92.40	7.20	6.16	3.48
23	97.18	7.74	3.48	6.50
24	101.73	7.74	6.16	10.83
25	114.57	11.23	6.16	7.17
26	117.32	10.81	6.16	6.50
27	121.53	9.97	3.48	7.70
28	180.00	12.32	6.16	6.16

Table A3: Configuration for bound defects for rare earth ions $R_{Cd(2)}^{\bullet} + R_{Cd(2)}^{\bullet} + V_{Cd(1)}^{''}$. The table associates the angles with the distances between the ions involved for the creation of the defects, with the values of the solution energies at 0 K and 300 K.

Configuration		I	II	III	IV	V	VI	VII	VIII	IX	X	XI
Ce (eV)	0 K	0.916	0.993	1.147	1.141	1.013	1.079	0.993	0.923	0.952	0.879	0.722
	300 K	0.717	0.786	0.940	1.052	0.806	0.867	0.854	0.725	0.756	0.682	0.527
Dy (eV)	0 K	1.182	1.231	1.391	1.388	1.293	1.345	1.226	1.186	1.191	1.155	0.984
	300 K	1.004	1.044	1.205	1.321	1.107	1.152	1.109	1.010	1.015	0.978	0.810
Er (eV)	0 K	1.259	1.302	1.462	1.463	1.370	1.419	1.296	1.263	1.263	1.234	1.061
	300 K	1.085	1.119	1.279	1.399	1.187	1.229	1.183	1.091	1.091	1.061	0.890
Eu (eV)	0 K	1.078	1.137	1.297	1.290	1.188	1.245	1.133	1.082	1.096	1.047	0.880
	300 K	0.892	0.943	1.103	1.215	0.994	1.045	1.009	0.899	0.913	0.863	0.699
Gd (eV)	0 K	1.111	1.167	1.327	1.321	1.222	1.278	1.163	1.116	1.127	1.082	0.914
	300 K	0.929	0.975	1.136	1.250	1.031	1.080	1.041	0.935	0.946	0.901	0.735
Ho (eV)	0 K	1.212	1.259	1.419	1.417	1.324	1.374	1.253	1.216	1.220	1.186	1.014
	300 K	1.036	1.073	1.234	1.352	1.139	1.183	1.138	1.042	1.045	1.011	0.841
Lu (eV)	0 K	1.406	1.443	1.603	1.606	1.517	1.561	1.435	1.409	1.403	1.383	1.205
	300 K	1.284	1.312	1.472	1.592	1.386	1.423	1.375	1.289	1.282	1.261	1.086
Nd (eV)	0 K	1.002	1.071	1.230	1.221	1.109	1.171	1.070	1.007	1.029	0.967	0.805
	300 K	0.810	0.872	1.032	1.140	0.910	0.966	0.939	0.818	0.841	0.778	0.618
Pr (eV)	0 K	1.000	1.069	1.227	1.219	1.106	1.168	1.067	1.005	1.027	0.965	0.803
	300 K	0.807	0.869	1.028	1.137	0.906	0.962	0.936	0.815	0.837	0.775	0.615
Sm (eV)	0 K	1.045	1.108	1.268	1.260	1.154	1.213	1.106	1.050	1.067	1.012	0.848
	300 K	0.858	0.913	1.073	1.183	0.959	1.012	0.979	0.864	0.882	0.827	0.665
Tb (eV)	0 K	1.146	1.200	1.361	1.354	1.259	1.313	1.195	1.150	1.159	1.117	0.948
	300 K	0.966	1.011	1.173	1.285	1.071	1.118	1.077	0.972	0.981	0.938	0.772
Tm (eV)	0 K	1.312	1.352	1.511	1.514	1.423	1.470	1.345	1.316	1.314	1.289	1.114
	300 K	1.141	1.172	1.331	1.453	1.243	1.283	1.235	1.147	1.144	1.119	0.946
Y (eV)	0 K	1.248	1.293	1.455	1.454	1.361	1.410	1.287	1.252	1.254	1.222	1.048
	300 K	1.097	1.133	1.295	1.413	1.201	1.244	1.197	1.103	1.105	1.072	0.901
Yb (eV)	0 K	1.329	1.368	1.527	1.531	1.439	1.485	1.360	1.333	1.329	1.306	1.130
	300 K	1.201	1.231	1.390	1.513	1.303	1.342	1.294	1.207	1.203	1.179	1.005